Volumetric aberrancy to map subtle faults and flexures

Xuan Qi[1] and Kurt Marfurt[1]

Abstract

One of the key tasks of a seismic interpreter is to map lateral changes in surfaces, not only including faults, folds, and flexures, but also incisements, diapirism, and dissolution features. Volumetrically, coherence provides rapid visualization of faults and curvature provides rapid visualization of folds and flexures. Aberrancy measures the lateral change (or gradient) of curvature along a picked or inferred surface. Aberrancy complements curvature and coherence. In normally faulted terrains, the aberrancy anomaly will track the coherence anomaly and fall between the most positive curvature anomaly defining the footwall and the most negative curvature anomaly defining the hanging wall. Aberrancy can delineate faults whose throw falls below the seismic resolution or is distributed across a suite of smaller conjugate faults that do not exhibit a coherence anomaly. Previously limited to horizon computations, we extend aberrancy to uninterpreted seismic data volumes. We apply our volumetric aberrancy calculation to a data volume acquired over the Barnett Shale gas reservoir of the Fort Worth Basin, Texas. In this area, the Barnett Shale is bound on the top by the Marble Falls Limestone and on the bottom by the Ellenburger Dolomite. Basement faulting controls karstification in the Ellenburger, resulting in the well-known "string of pearls" pattern seen on coherence images. Aberrancy delineates small karst features, which are, in many places, too smoothly varying to be detected by coherence. Equally important, aberrancy provides the azimuthal orientation of the fault and flexure anomalies.

Introduction

Well-known to mathematicians (Schot, 1978), aberrancy has only recently been applied to 3D seismic surveys. Gao (2013) defines aberrancy as a measure of the deformation of a surface. Aberrancy measures the lateral change (or gradient) of the curvature of a picked or inferred surface. In 3D, aberrancy is a vector described by its magnitude and azimuth. The magnitude defines the intensity of surface deformation, whereas the azimuth indicates the direction in which the curvature decreases in signed value. This positive-to-negative definition provides as azimuth consistent with that of fault-plane azimuths.

Gao and Di (2015) find aberrancy to be complementary to curvature. In normally faulted terrains, the aberrancy anomaly will track the coherence anomaly and fall between the most positive curvature anomalies defining the footwall and the most negative curvature anomalies defining the hanging walls (Chopra and Marfurt, 2007b). Unlike coherence, which measures lateral changes in waveform and/or amplitude, aberrancy measures lateral changes in curvature, and as such provides not only an indication of the strength of the normal faulting (the magnitude of the vector), but also the direction of the downthrown side (the azimuth of the vector). The value of aberrancy is that it may delineate faults whose throw falls below seismic resolution, or is distributed across a suite of smaller conjugate faults, which do not exhibit a coherence anomaly (Di and Gao, 2016) (Figure 1). For this reason, we hypothesize that aberrancy will be quite useful in correlating surface seismic data to fractures associated with faults that are commonly seen in image logs from horizontal wells.

Because aberrancy measures the changes in curvature, it characterizes third-order surface behavior (Joshi and Séquin, 2010). Calculation of aberrancy involves two main challenges: the robustness of high-order derivatives and computational efficiency. Di and Gao (2014) introduce a horizon-based aberrancy calculation based on first computing third derivatives at equal azimuthal intervals. They then search these values for extrema. More recently, Di and Gao (2016) show how rotating the coordinate system can simplify the equations. We build on this latter innovation and generalize it to compute aberrancy volumetrically. We compute second derivatives of vector dip in the x-, y-, and z-directions, rotate the calculations about the local vector dip to simplify the computation, compute aberrancy, and then rotate the aberrancy vectors back the original coordinate system. In general, there are three roots to

[1]University of Oklahoma, Conoco Phillips School of Geology and Geophysics, Norman, Oklahoma, USA. E-mail: sherryqixuan@ou.edu; kmarfurt@ou.edu.

Manuscript received by the Editor 29 June 2017; revised manuscript received 10 October 2017; published ahead of production 24 January 2018; published online 19 March 2018. This paper appears in *Interpretation*, Vol. 6, No. 2 (May 2018); p. T349–T365, 22 FIGS.

http://dx.doi.org/10.1190/INT-2017-0114.1.

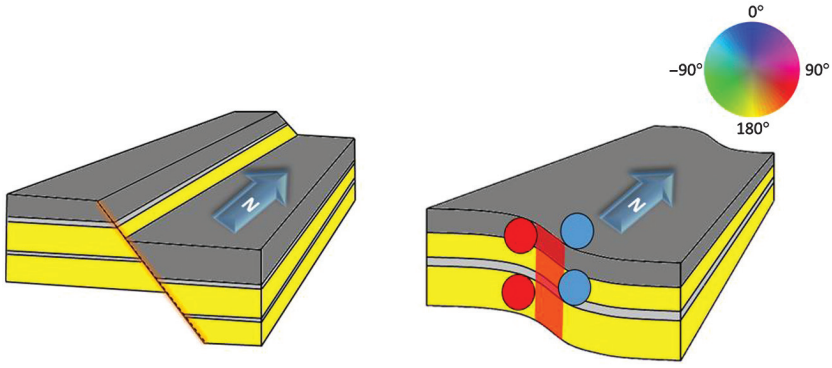

Figure 1. Cartoons of two different fault models, (a) a model in which finite offset across a fault results in a strong coherence anomaly but no curvature or aberrancy anomaly. (b) A model in which the offset is distributed over a zone of conjugate faults, such that the now-continuous reflector no longer gives rise to a coherence anomaly. Positive curvature anomalies on the footwall are indicated by red circles, whereas negative curvature anomalies on the hanging wall are indicated by the blue circles. Aberrancy measures the change in curvature, which in this example is toward the east, and it is displayed as a magenta-red aberrancy anomaly.

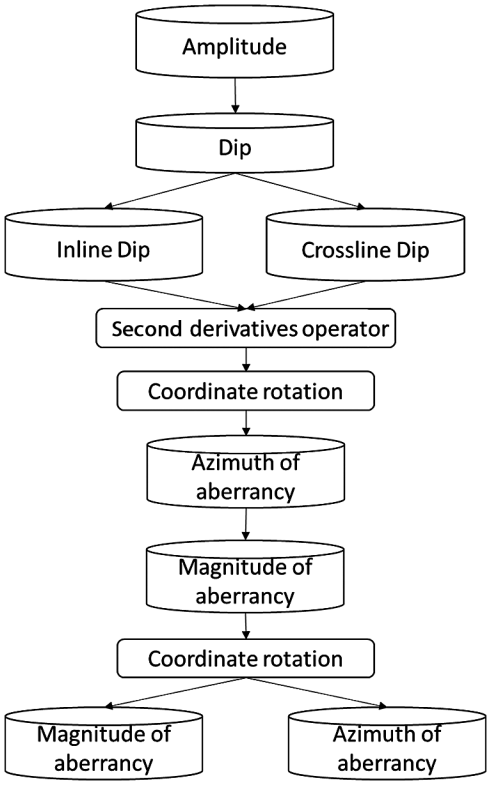

Figure 2. The internal steps of aberrancy computation. The first step is to compute the inline and crossline dip, which includes the first and second derivatives of inline and crossline dip. The second step is to rotate the original coordinate system, x_0-y_0-z_0, to the new coordinate system,x_1-y_1-z_1 by using the dip magnitude and dip azimuth. The third step is to find extrema of a cubic function, which compute the magnitude and azimuth of aberrancy. The final step is rotate the new coordinate sytem back to original coordinate system to get the correct aberrancy azimuth value.

the third-order differential equation (Di and Gao, 2016), which we define as the maximum aberrancy, the minimum aberrancy, and the intermedium aberrancy.

We begin this paper by summarizing the theory of aberrancy. Then, we apply our volumetric aberrancy calculation to two synthetic models: a 3D synthetic of a circular sinkhole model and a 3D synthetic consisting of an east–west-trending flexure and three north–south-trending flexures. Next, we apply our volumetric aberrancy algorithm to a data volume acquired over the Barnett Shale gas reservoir of the Fort Worth Basin (FWB), Texas. We conclude with a summary of interpretational value of the attribute as well as the computational cast mathematical details for those wishing to implement such an algorithm are provided in the appendices.

Theory

Apparent dip, curvature, and aberrancy

Geoscientists define a locally planar surface by its dip magnitude θ and dip azimuth ϕ, where θ is sometimes called the true dip to distinguish it from the apparent dip at an azimuth β. Introducing the dip vector $\mathbf{p}$, measured in dimensionless units of km/km or kft/kft, the components of the true dip along the x_1- and x_2-axes are

$$p_1 = \tan\theta\cos\varphi, \quad p_2 = \tan\theta\sin\varphi, \tag{1}$$

whereas the apparent dip component p_β and apparent dip angle θ_β along the azimuth β are

$$p_\beta = \tan\theta\cos\beta, \quad \theta_\beta = \tan^{-1}p_\beta. \tag{2}$$

Most geoscientists are also familiar with the two principal (most positive and most negative) curvature values k_1 and k_2 and their corresponding strikes γ_1 and γ_2, which Rich and Marfurt (2013) show are the eigenvalues and eigenvectors of a solid geometry problem. Somewhat less known is the apparent curvature at a given azimuth, or Euler curvature k_β, at strike β, defined as

$$k_\beta = k_1\cos^2(\beta-\gamma_1) + k_2\sin^2(\beta-\gamma_1). \tag{3}$$

Di and Gao (2014) show that one can compute the most positive and most negative principal curvatures by searching for extrema of the Euler or apparent curvatures. This search is significantly simplified if one first locally flattens the data about the vector dip at the analysis point. Although this approach is somewhat less efficient than the more commonly used eigenvector curvature solution, it provides not only physical insight into the meaning of the principal curvatures, but also a means to compute the extrema of aberrancy.

Because the vector dip at any voxel can be different from its neighbors, a direct implementation of Di and Gao's (2014) algorithm would require rotating an analysis window of volumetric dip values **p**, followed by the computation of its derivatives using a convolution operator. In our implementation, this convolution operator typically uses 121 traces and 50 vertical samples, or a computational stencil of 6050 points, which would not be amenable to vector-computing strategies. Therefore, we compute the required derivatives in the original unrotated coordinate system, and then we obtain the corresponding derivatives in the locally rotated coordinate system through three cascaded rotation operators applied to the $3 \times 3 \times 3$, or 27-element second derivative operators applied to the three vector dip components (Figure 2). These details are important to those who wish to implement aberrancy, but they provide only limited insight into its use and are thus relegated to Appendix A.

After rotation, one can compute the apparent aberrancy at any azimuth ψ in the rotated plane, using the following equation:

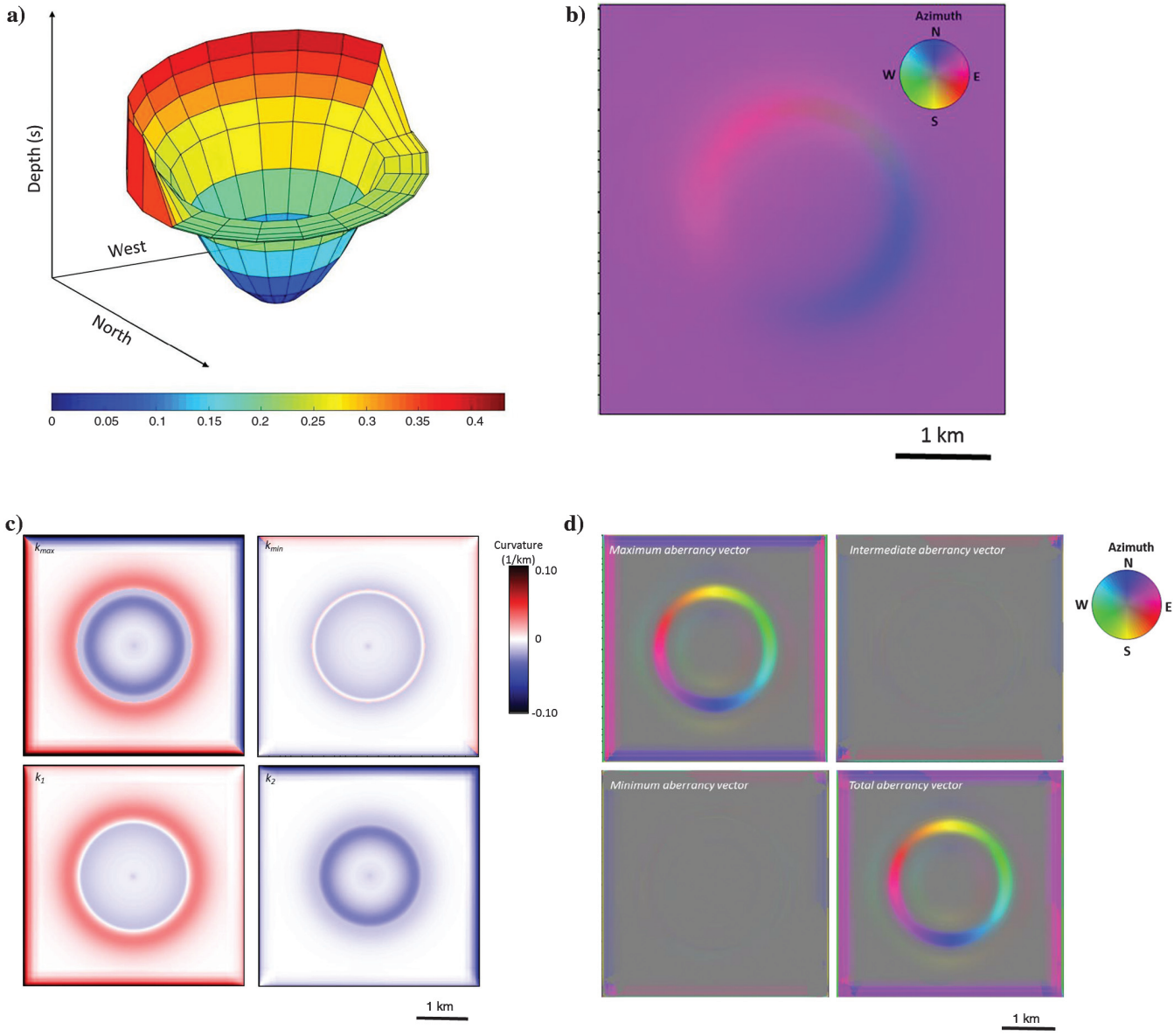

Figure 3. (a) Mesh grid showing a simple synthetic model in depth consisting of a circular sinkhole embedded in a planar reflector dipping 2° to the northeast. (b) Vector dip computed from the synthetic model shown in (a). The maximum dip of the sink is 2°, such that the edge dips 4° to the northeast in the southwest portion of the sinkhole and dips 0° or is nearly flat in the northeast portion of the sinkhole. (c) Alternative means of displaying the two extreme curvature values computed from the synthetic shown in the previous figure. In this image, the minimum curvature carries little information because the input model consists of parallel rather than crossing flexures. (d) Time slices through the aberrancy volumes corresponding to the synthetic dip and curvature images shown in the previous two figures. The total aberrancy is the vector sum of the maximum, intermediate, and minimum aberrancy vectors.

$$f_\psi = \frac{\partial^3 z'}{\partial x_1' \partial x_1' \partial x_1'} \cos^3\psi + 3\frac{\partial^3 z'}{\partial x_1' \partial x_1' \partial x_2'} \cos^2\psi \sin\psi + 3\frac{\partial^3 z'}{\partial x_1' \partial x_2' \partial x_2'} \cos\psi \sin^2\psi + \frac{\partial^3 z'}{\partial x_2' \partial x_2' \partial x_2'} \sin^3\psi, \quad (4)$$

where the primes indicate the surface $z'(x_1', x_2')$ in the rotated coordinate system. For volumetric aberrancy, one does not explicitly pick surfaces, but rather computes the first derivatives of the assumed surfaces, resulting in the volumetric dip component volumes p_1 and p_2 defined in equation. Equation 4 then becomes

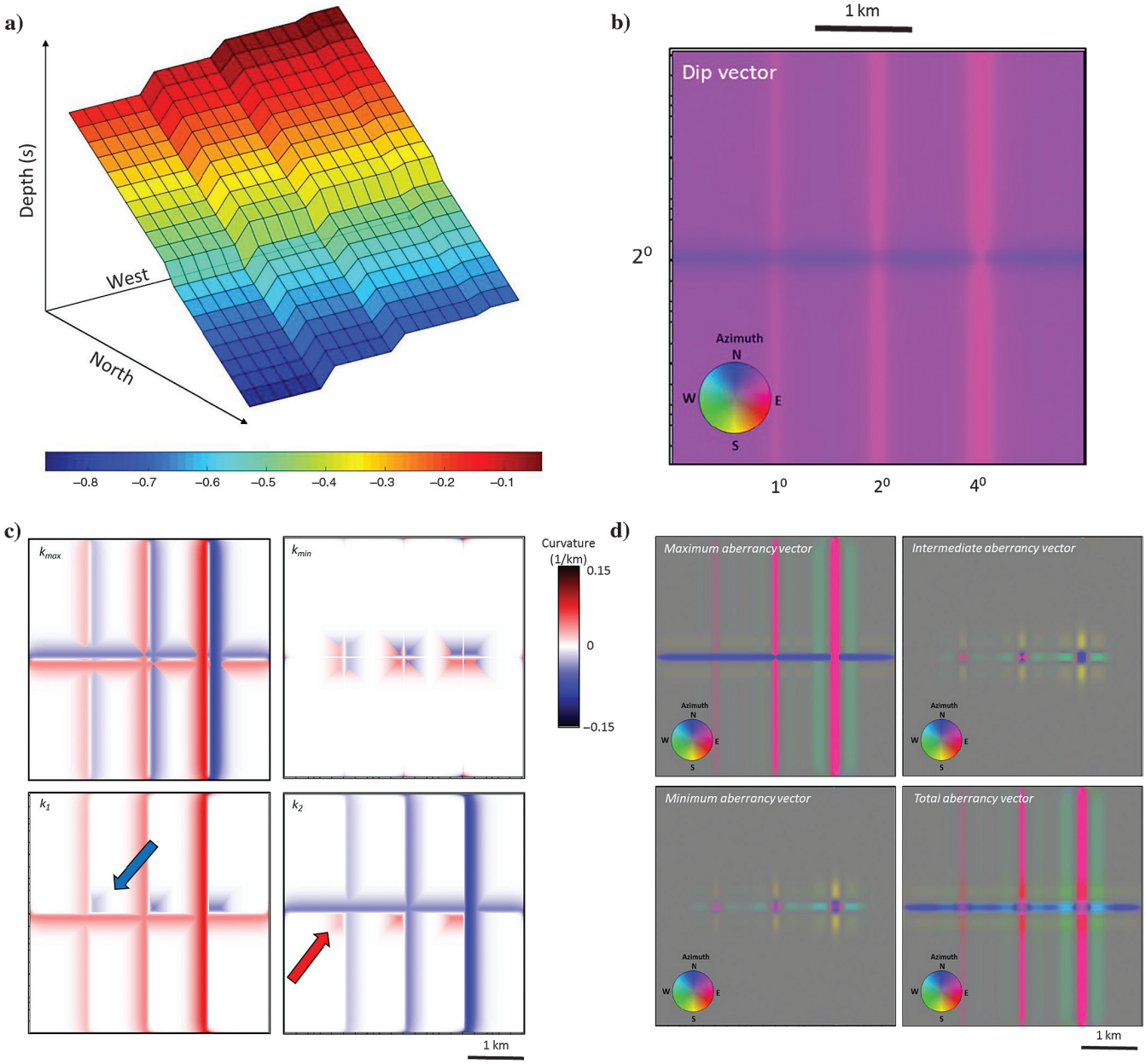

Figure 4. (a) Mesh grid showing a simple synthetic model in depth consisting of an east–west-trending flexure and three north–south-trending flexures. (b) Vector dip computed from the synthetic model is shown in (a). The east–west-trending flexure dipping to the north appearing as blue, and three north–south-trending flexures dipping toward the east and appearing as magenta-red. The maximum dip for each of the north–south flexures is 1°, 2°, and 4°, crossing the east–west flexure with maximum dip of 2°. (c) Alternative means of displaying the two extreme curvature values computed from the synthetic shown in the previous figure. (d) Time slices through the aberrancy volumes corresponding to the synthetic dip and curvature images shown in the previous two figures. The total aberrancy is the vector sum of the maximum, intermediate, and minimum aberrancy vectors.

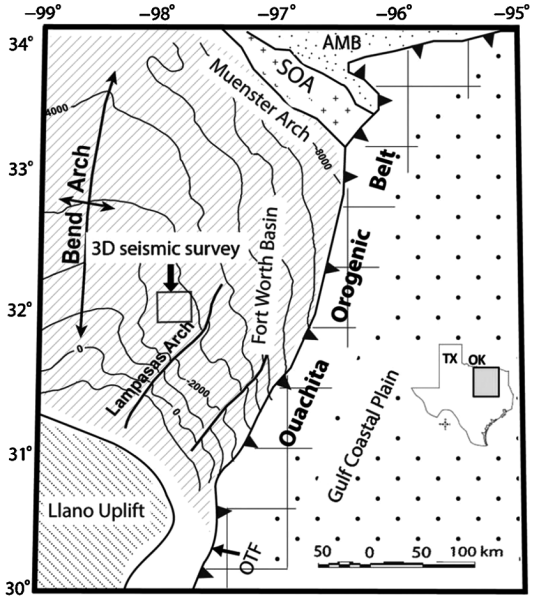

Figure 5. Index map of FWB and major tectonic units (modified after Khatiwada et al., 2013) corresponding to the gray square in the map of Texas.

$$f_\psi = \frac{\partial^2 p_1'}{\partial x_1' \partial x_1'}\cos^3\psi + \frac{3}{2}\left(\frac{\partial^2 p_1'}{\partial x_1' \partial x_2'} + \frac{\partial^2 p_2'}{\partial x_1' \partial x_1'}\right)\cos^2\psi \sin\psi + \frac{3}{2}\left(\frac{\partial^2 p_1'}{\partial x_2' \partial x_2'} + \frac{\partial^2 p_2'}{\partial x_1' \partial x_2'}\right)\cos\psi \sin^2\psi + \frac{\partial^2 p_2'}{\partial x_2' \partial x_2'}\sin^3\psi. \quad (5)$$

The extrema of the aberrancy are computed by minimizing the value of f_ψ with respect to ψ. Recall that the vector dip is computed using the first derivative of the surface z and has one extrema, the dip magnitude and the dip azimuth, which define a single dip vector. Curvature is computed using the second derivatives of the surface z and has two extrema, the most positive and most negative principal curvatures and their strikes. Aberrancy is computed using the third derivatives (equation 4) of surface z, and therefore will have in general three extrema. We will call these extrema the maximum, intermediate, and minimum aberrancy vectors expressed by its magnitude f_ψ and its azimuth ψ (Borwein and Erdélyi, 2012). The numerical roots of

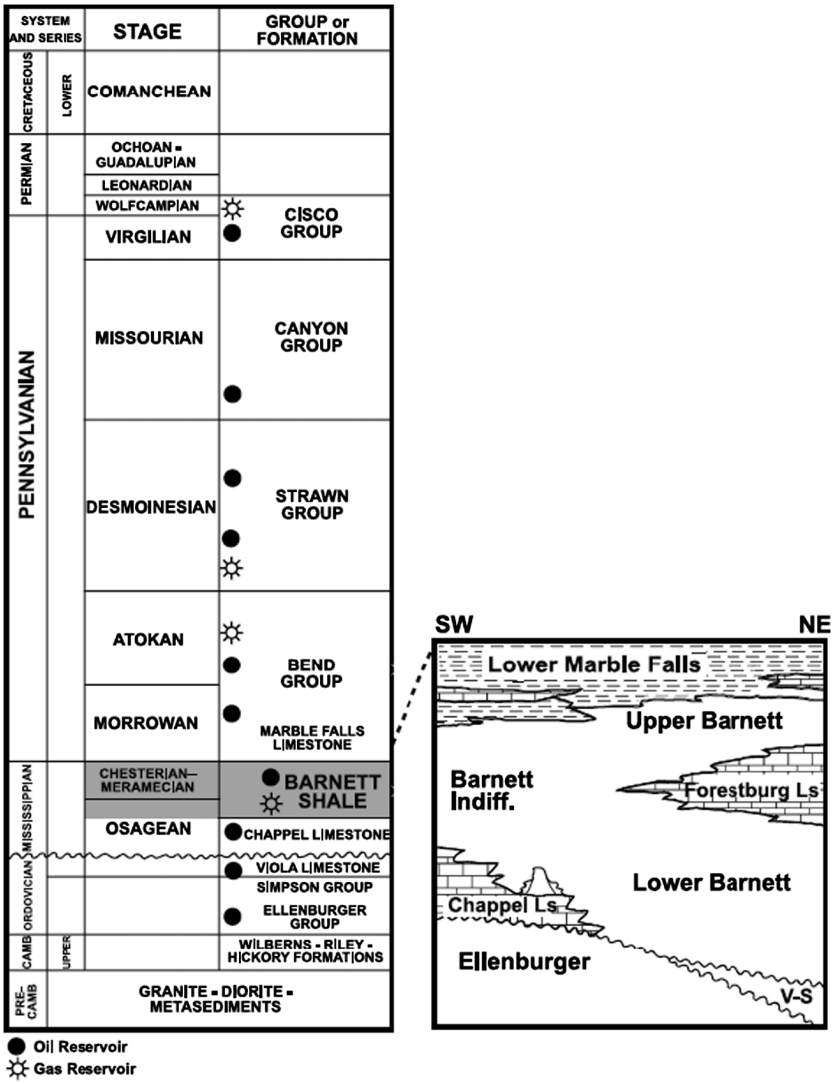

Figure 6. Generalized stratigraphic column (modified from Montgomery et al., 2005).

the minimization problem are in terms of tan ψ (equation B-1), such that initially ψ ranges between $\pm 90°$. Inserting these roots into equation 5 may provide negative values of aberrancy f_ψ. It is obvious that a negative flexure to the north is equivalent to a positive flexure to the south. For this reason, in our implementation, we define our resulting maximum, intermediate, and minimum aberrancy magnitudes, $f_{\max}$, f_{int}, and $f_{\min}$, to be strictly positive, with the corresponding azimuths $\psi_{\max}$, ψ_{int}, and $\psi_{\min}$ ranging between $\pm 180°$. The analysis and display of three roots can be cumbersome, although we hypothesize nonzero values of f_{int}, and $f_{\min}$, represent intersecting flexures, which may be indicators of increased shear strain. We leave such quantitative analysis to future work, which will require image logs calibration. In this paper, we will examine the total vector aberrancy vector $\mathbf{f_{tot}}$, which is simply the sum of the three aberrancy vectors:

$$\mathbf{f_{tot}} = \mathbf{f_{max}} + \mathbf{f_{int}} + \mathbf{f_{min}}. \tag{6}$$

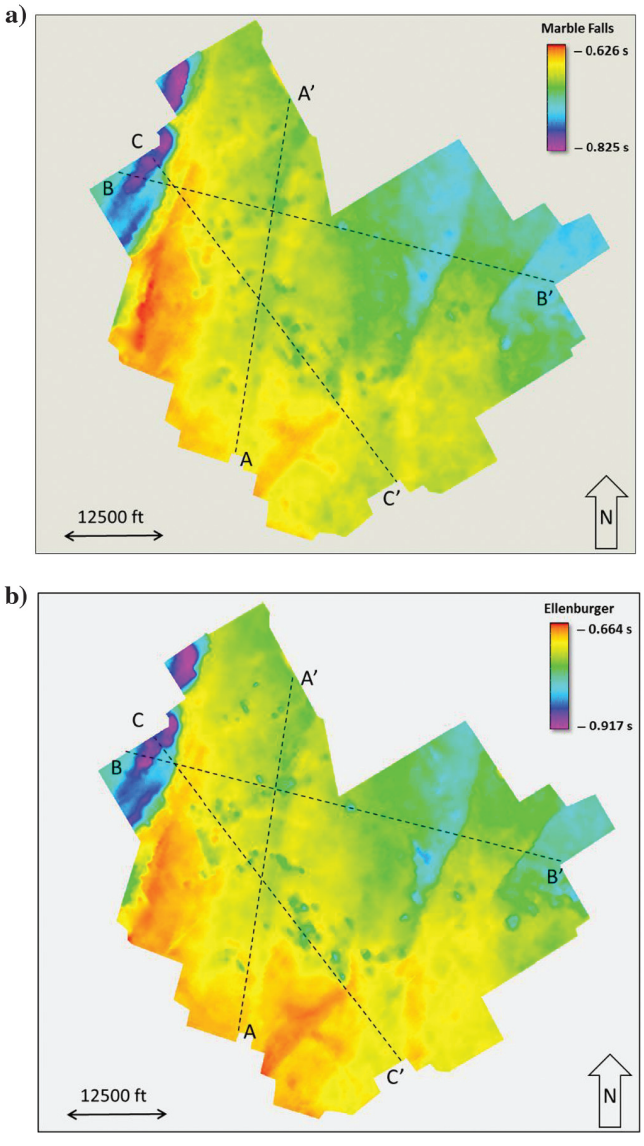

Figure 7. (a) Time structure maps of the top Marble Falls and (b) Ellenburger horizons with three crosslines AA′, BB′, and CC′. Vertical slices AA′, BB′, and CC′ will be discussed in subsequent figures.

Synthetic calibration

A 3D synthetic of a circular sinkhole model

Figure 3 shows a simple 3D synthetic circular model used to validate the aberrancy calculation. The synthetic consists of a circular sinkhole embedded in a planar reflector dipping 2° to the northeast. In this example, the intermediate and minimum aberrancy vectors are near zero. Note that, the total aberrancy vector is oriented inwards toward the center of the sinkhole. Also, note that the maximum and total aberrancy vectors sit in the approximately middle of the most positive curvature and the most negative curvature (Figure 3b), where we observe the largest changes in the magnitude of curvature (Figure 3c).

A 3D synthetic consisting of an east–west-trending flexure and three north–south-trending flexures

To calibrate how aberrancy works when two flexures cross each other, we built the simple synthetic model shown in Figure 4a, consisting of an east–west-trending flexure (dipping to the north and appearing as blue), and three north–south-trending flexures (dipping toward the east and appearing as red-magenta). The maximum dip of north–south flexures increases from 1° to 3° from left to right.

Rich and Marfurt (2013) show how the principal curvatures are the solution of an eigenvector problem. The first eigenvalue corresponds to the eigenvector that best represents the deformation at any voxel, and thus it is the one exhibiting the largest absolute value $k_{\max}$. The second eigenvector represents the deformation in the orthogonal direction and is denoted as $k_{\min}$. Note that the patterns exhibited by the weaker flexures (the north–south one on the left, and the east–west one on the right) are broken by the locally larger flexures (Figure 4b). Such images make it more difficult to track weak faults cut by stronger faults. In contrast, the most positive and most negative principal curvatures k_1 and k_2 exhibit more continuous pattern. The blue arrow indicates a bowl-shaped anomaly in the most positive curvature slice, whereas the red arrow indicates a dome-shaped anomaly in the most-negative curvature image (Figure 4b).

After examining the maximum, intermediate, and minimum aberrancy vectors, we find that the total aberrancy vector provides a single vector volume appropriate for structural interpretation (Figure 4c). However, the intermediate and minimum aberrancy indicate zones of conflicting flexure, and, depending on the tectonic model, may potentially show areas of more intense natural fracturing.

Application

Geologic background

The FWB is a shallow, north–south-elongated foreland basin extending 38,100 km^2 (15,000 mi^2) in north-central Texas (Montgomery et al., 2005). The Ouachita thrust-fold belt, Llano uplift, Bend arch, and the Muenster arch bound the basin to the east, south, west, and north, correspondingly (Figure 5). Preserved fill in the FWB reaches a maximum of approximately 3660 m (12,000 ft) in the northeast corner, adjacent to the

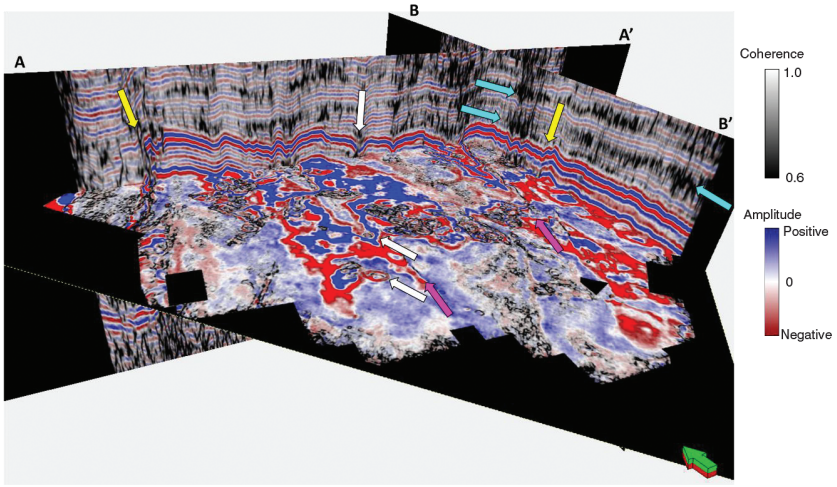

Figure 8. Vertical slices AA′ and BB′ through the Barnett Shale interval through the corendered seismic amplitude and coherence volumes. Time slice at the Barnett Shale level ($t = 0.726$) through the coherence volume. Yellow arrows indicate two faults delineated on lines AA′ and BB′ that continue into the time slice. Even though the seismic amplitude data have been preconditioned, there are several strata-bound low-coherence anomalies (cyan arrows), some of which are associated with deeper collapse features (white arrows), and others with low signal-to-noise ratio.

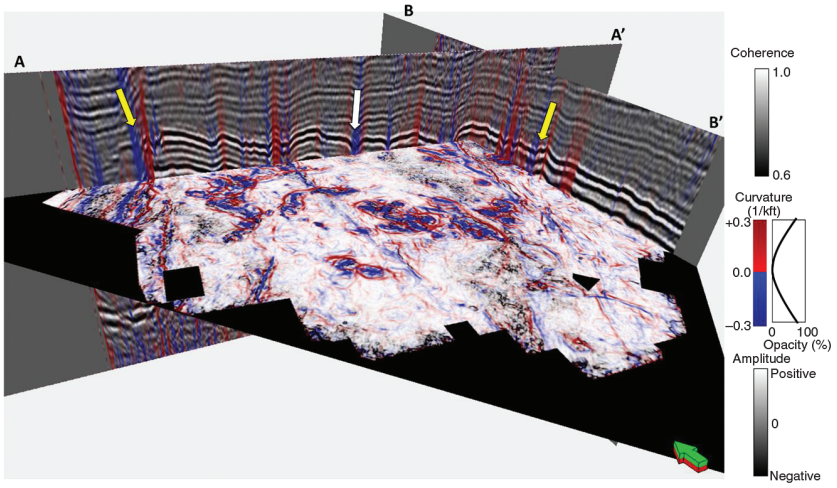

Figure 9. The same slices shown in the previous figure, but now through the corendered most-positive and most-negative curvatures with seismic amplitude on the vertical slices and with coherence on the time slice. The yellow arrows indicate the same faults shown indicated in the previous image. The white arrow points at the deeper collapse features.

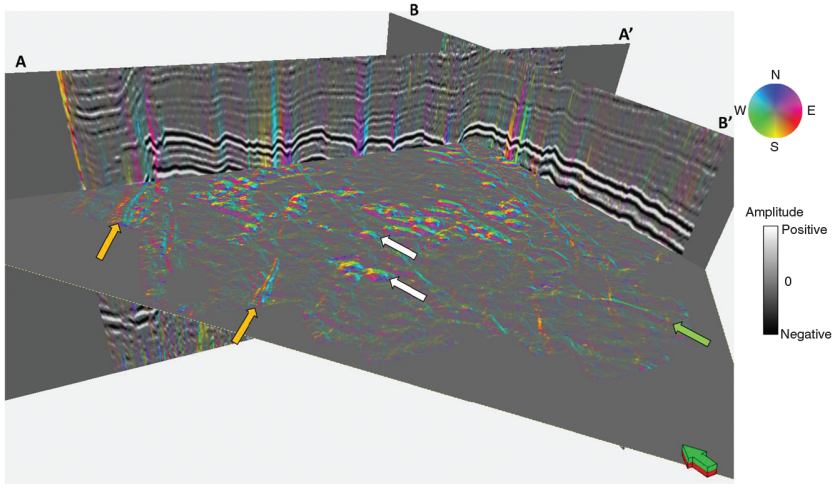

Figure 10. The same slices shown in the previous two figures through the total aberrancy volume. Note the continuous flexures cutting through the time slice. Orange arrows indicate couplets, defining the edges of small grabens by a northwest-oriented (cyan) flexure on one side and a southeast-oriented (orange) flexure on the other. The green arrow indicates a graben delineated by a northeast-oriented (magenta) on one side and a southwest-oriented (lime green) flexure on the other. Several of the collapse features exhibit flexures that cycle the color wheel (white arrows).

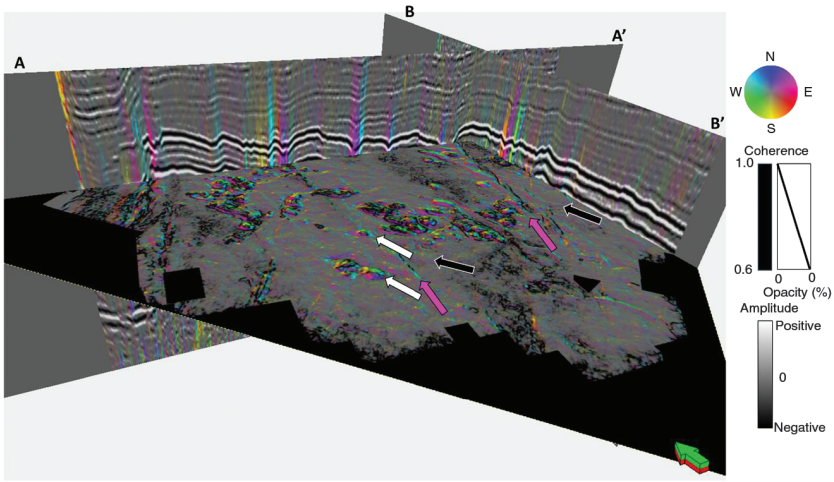

Figure 11. The same slices as the previous four figures, but now with the time slice through corendered aberrancy vector and coherence volumes. The magenta arrows indicate the same two faults shown in the previous image. The flexures indicated by the black arrows exhibit a different azimuth, suggesting transtensional deformation. In this example, coherence is complementary to aberrancy, providing additional insight into the interpretation. White arrows indicate the same two collapse features shown in previous images. In this example, aberrancy confirms an interpretation already made by examining coherence alone.

Muenster arch (Montgomery et al., 2005). Deposits consist of approximately 1200–1500 m (4000–5000 ft) of Ordovician-Mississippian carbonates and shales, 1800–2100 m (6000–7000 ft) of Pennsylvanian clastics and carbonates, and, in the eastern parts of the basin, a thin layer of Cretaceous rocks (Montgomery et al., 2005).

The structures in the FWB include major and minor faulting, local folding, fracturing, and karst-related collapse features (Montgomery et al., 2005; Qi et al., 2014). Thrust-fold structures are more common in the easternmost parts of the basin. Studies have shown that the major fault exerted significant control on the depositional patterns and thermal history of the Barnett (Qi et al., 2014). The small-scale faulting controls karstification in the Ellenburger, resulting in the well-known "string of pearls" pattern seen on seismic coherence images (Schuelke, 2011).

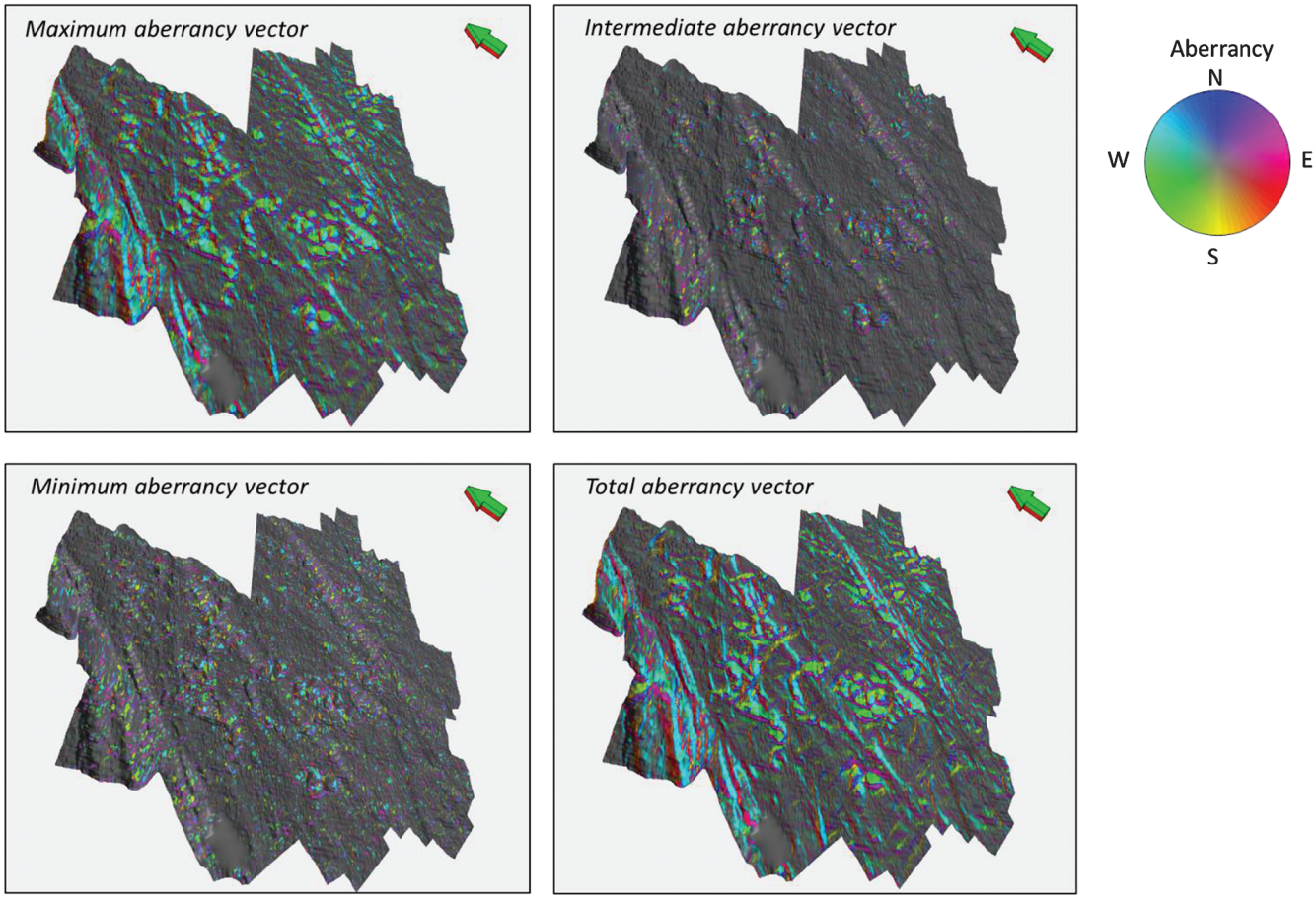

Figure 12. Horizon slices along the top Marble Falls through the aberrancy volumes. The total aberrancy is the vector sum of the maximum, intermediate, and minimum aberrancy vectors. We find the total aberrancy vector to be most useful for structural interpretation; however, the intermediate and minimum aberrancy indicate zones of conflicting flexure, and depending on the tectonic model, they may potentially indicate areas of more intense natural fracturing.

The Barnett Shale of the FWB, Texas, has played an important role in a gas-shale play in North America. Recent studies estimate that the Barnett Shales may hold as much as 39 trillion cubic feet of gas undiscovered (Bruner and Smosna, 2011). The Barnett Shale of the FWB, Texas, formed during the late Paleozoic Ouachita Orogeny, generated by the convergence of Laurasia and Gondwana (Bruner and Smosna, 2011). Figure 6 provides a generalized stratigraphy column of the FWB. The Barnett Shale is an organic-rich, petroliferous black shale of middle-late Mississippian age, bound in the survey between the Lower Marble Falls and Ellenburger Group (Figure 6). The Marble Falls Formation is conformably overlying the Barnett Shale on top. It typically includes two parts, an upper limestone interval and a lower member of interbedded dark limestone and gray-black shale (Montgomery et al., 2005). The top of the Ellenburger Group is an erosional surface (second-order Sauk-Tippecanoe erosional unconformity) commonly characterized by solution-collapse features (Montgomery et al., 2005). We expect to see major and/or minor faulting, local folding, fracturing, and karst-related collapse features within our study area.

Seismic data

In 2006, Marathon Oil Company acquired a 3D wide-azimuth seismic survey to image the Barnett Shale using 16 live receiver lines with a nominal 16×16 m (55×55 ft) CDP bin size (Khatiwada et al., 2013). The overall data quality is excellent, with a poststack data-conditioning workflow, including edge-preserving structure oriented filtering and spectral balancing performed by Qi et al. (2014), further improving the continuity and vertical resolution. The top Marble Falls Limestone is an easy-to-pick horizon that lies immediately above the Barnett Shale at approximately 0.7 s two-way time.

Results

Seismic amplitude

Seismic amplitude is the most commonly used attribute in seismic interpretation. Lines AA′ and BB′ (Figure 8) show two strong reflections, representing the top of the Marble Falls (Figure 7a) and the top of Ellenburger Group (Figure 7b). The organic-rich Barnett Shale sits between these two units, with the arrows indicating karst collapse features. At least two major faults control the collapse features indicated by yellow arrows. Several smaller compaction induced sags are

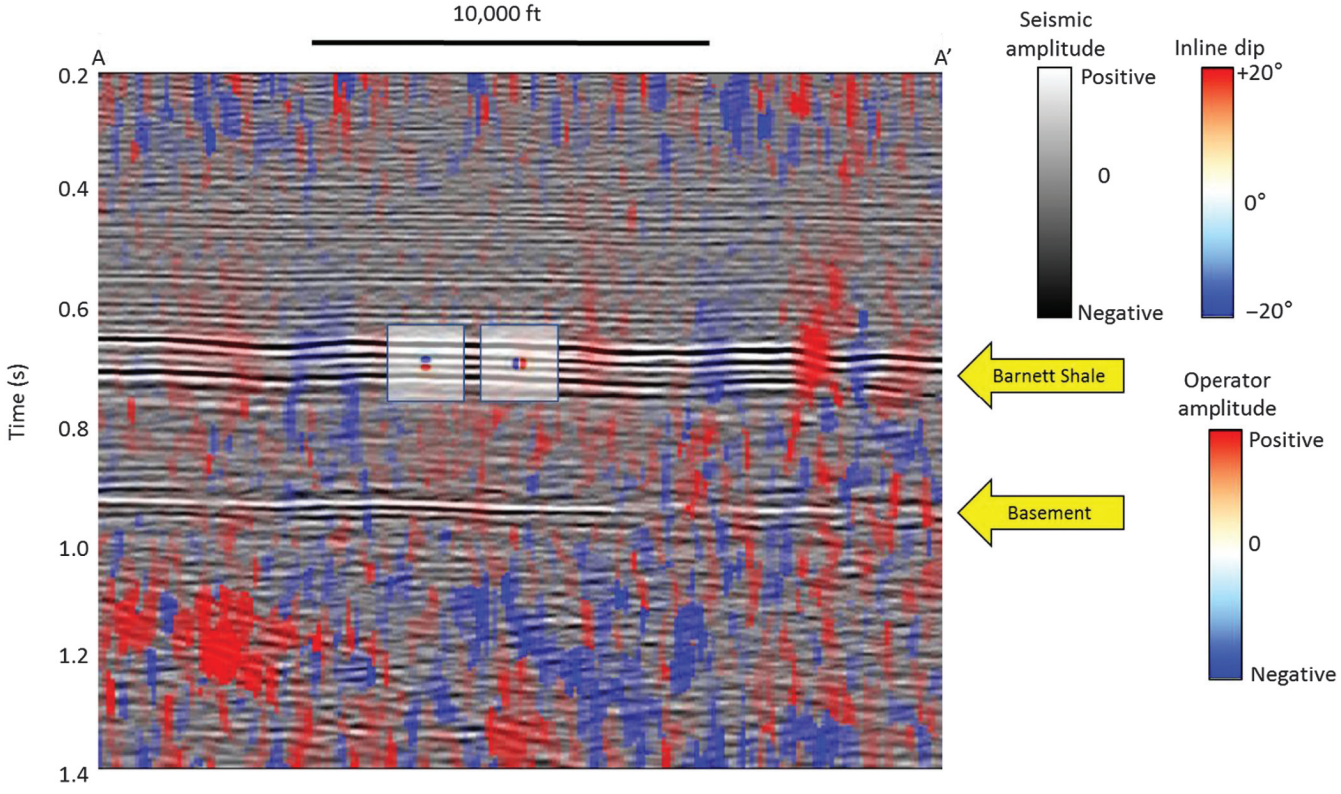

Figure 13. Vertical slice along line AA′ through the seismic amplitude corendered with the inline component of the vector dip at approximately 1:1 vertical to the horizontal aspect ratio, showing the data quality. The location of the line is shown in Figure 14a. There is strong acquisition footprint in the shallow section at $t = 0.3$s, resulting in vertical stripes in the inline dip. In contrast, the inline dip estimated at the target Barnett Shale level at $t = 0.7$ s exhibits a high signal-to-noise ratio. The top of the basement is at $t = 0.9$ s in this image. Below this level, the reflectors become less continuous, resulting in a noisier estimation of the inline-dip component. The vertical (left square inset) and inline (right square inset) derivative operators show the extent of what we call a "long-wavelength" operator. Because the bin size is 33.5×33.5 m (110×110 ft), the crossline derivative operator (not shown) is a rotated version of the inline derivative operator for this data volume.

seen some distance away from the faults. Even though the seismic amplitude data have been preconditioned, there are several strata-bound low-coherence anomalies, some of which are associated with deeper collapse features (cyan arrows), and others are simply due to areas exhibiting a low seismic signal-to-noise ratio.

Coherence

Coherence measures the similarity between waveforms on neighboring traces, and helps to delineate faults and collapse features in the study area (Figure 9). Figures 8 and 9 show the same time slices at approximately $t = 0.726$ s through coherence volume. Time slices through the coherence volume show a complex system of lineaments and collapse features (yellow and white arrows). Although we do see the vertical trace of several faults, the most prominent features are the circular collapse features, which are more pronounced at the deeper Ellenburger level than at the Marble Falls level (Figure 7).

Curvature

When calibrated to image logs, most-negative and most-positive curvatures can serve as a means of predicting fractures from surface seismic data (Chopra and Marfurt, 2007a). Figure 9 shows corendered most-positive and most-negative curvatures, corendered with coherence on the time slice and with amplitude on the same vertical slice. Notice that the major faults exhibit a positive curvature anomaly on the footwall, which is laterally offset from a corresponding negative curvature anomaly on the hanging wall. The bowl-shaped collapse features exhibit a negative curvature value and appear as blue ellipses (white and yellow arrows).

Aberrancy

Because aberrancy measures the lateral change (or gradient) of the curvature along a picked or inferred surface, it not only detects major faults that exhibit finite displacement, but also more subtle "subseismic-resolution" faults that appears as flexures referring to Figure 1. Figure 1a shows a finite offset across a fault, which results in a strong coherence anomaly (highlighted in red). In contrast, in Figure 1b, if the offset is distributed over a zone of conjugate faults, where the offsets fall below seismic resolution. The continuous reflector no longer gives rise to a coherence anomaly. Aberrancy measures the change in curvature, highlight-

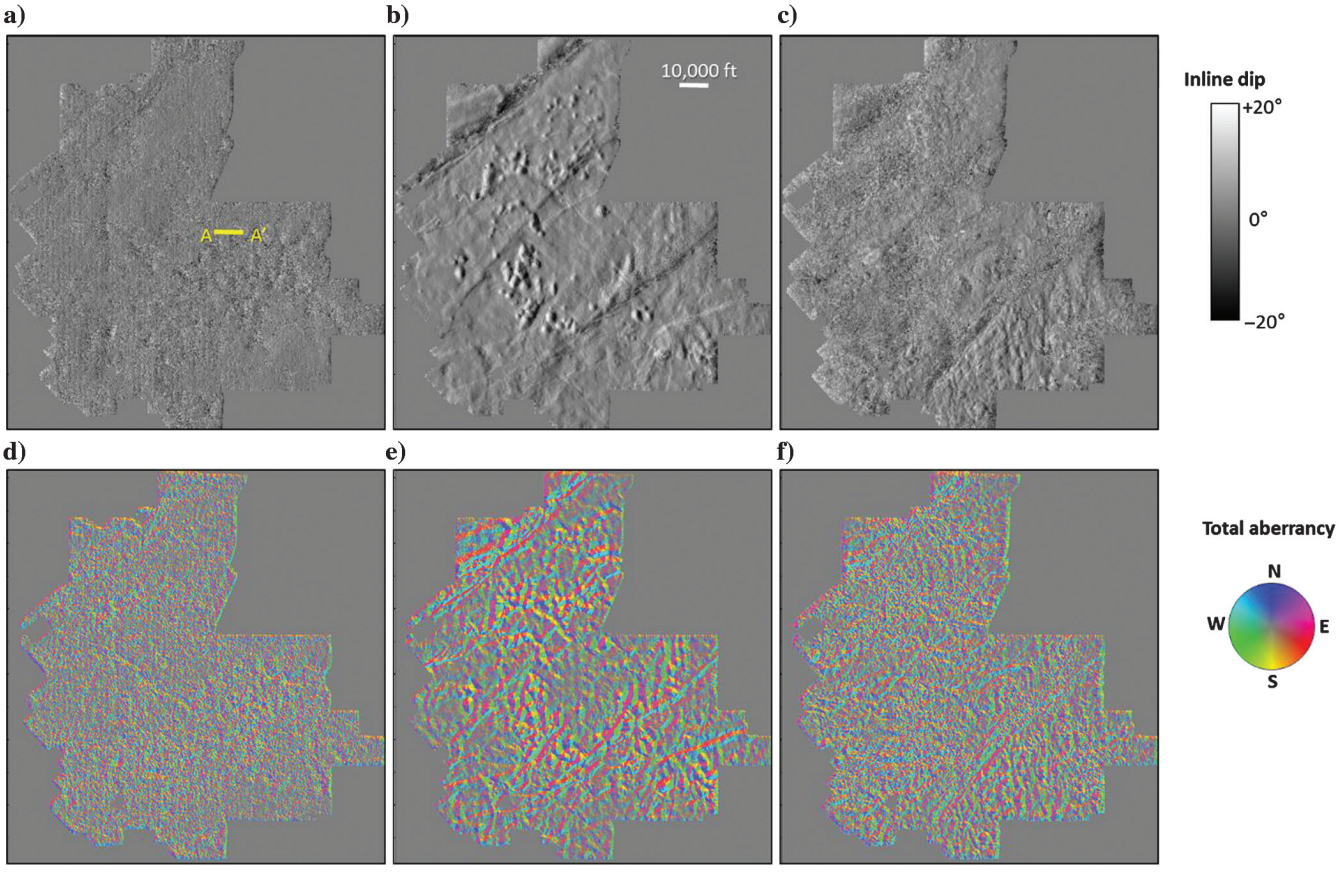

Figure 14. Time slices at (a) $t = 0.3$, (b) 0.7, and (c) 1.0 s through the inline component of the dip vector. Line AA′ indicates the location of the vertical slice through the same volume shown in the previous figure. Time slices through total vector aberrancy at (d) $t = 0.3$, (e) 0.7, and (f) 1.0 s. Because aberrancy is the second derivative of the two dip components, the time slice in (d) exhibits the acquisition footprint, whereas the time slice in (f) is noisy due to the poorly imaged basement reflectors. In contrast, the time slice in (e) at the target level exhibits a high signal-to-noise ratio and accurately delineates the faulting and karsting.

ing the zone of conjugate faults area that offset a horst block to the east (shaded in red). Figure 10 shows the same slices as in the previous two images, but now through the total aberrancy volume. Orange and green arrows indicate small grabens, whereas white arrows indicate collapse features. Figure 11 shows the same image, but now with the addition of coherence on the time slice. In this data volume, the inability of coherence to map subtle featues may be due to geology (a single fault becoming a flexure, fault splay) or data quality issues (limit of seismic resolution of a fault offset, or insufficient statics and velocities limiting the lateral resolution of the image). Figure 12 shows horizon slices along the top Marble Falls through the maximum, intermediate, minimum, and total aberrancy vectors. The total aberrancy vector provides a single vector volume appropriate for structural interpretation. Lineaments in the total aberrancy vector horizon slices indicate faults or flexures, whereas flexures that cycle the color wheel (as in the synthetic example shown in Figure 1) indicate collapse features. The intermediate and minimum aberrancy may indicate zones of conflicting flexure, and depending on the tectonic model, may potentially show areas of more intense natural fracturing.

Aberrancy is a function of signal-to-noise ratio (Figures 13 and 14). Note the strong northwest–southeast-trending acquisition footprint in the shallow slice shown in Figure 14a. Likewise, the dip estimate in the basement in Figure 14c is also noisy. In contrast, the time slice in Figure 14b through the target Barnett Shale area exhibits a high signal-to-noise ratio. The accuracy of the aberrancy estimates are directly related to the accuracy of the input components of the structural dip vector (Figure 14d–14f). The image in Figure 14a is contaminated by acquisition footprint, whereas that in Figure 14c is noisy, although useful structural lineaments can still be extracted in total aberrancy images.

Comparison between aberrancy and coherence on cross sections

To better understand the collapse patterns, flexures, faults, and their expression in the aberrancy attributes, we display three vertical cross sections through a seismic survey corresponding to lines AA′, BB′, and CC′ in Figures 15, 16, and 17. Aberrancy seems to be less sensitive to the chaotic zones seen in vertical sections AA′ and BB′, showing flexures that continue vertically through the section. In cross section AA′ the anomalies along the top Marble Falls that are better resolved by aberrancy (Figure 15). From left to right, aberrancy delineates flexures (indicated by green arrows), which coherence is unable to resolve. In cross section BB′, the faults in the aberrancy image appear as steeply dipping continuous thin lines, but as stair-step blotches in coherence image (Figure 16). Similarly, in cross section CC′, the collapse features are better resolved by aberrancy, indicated by green arrows (Figure 17).

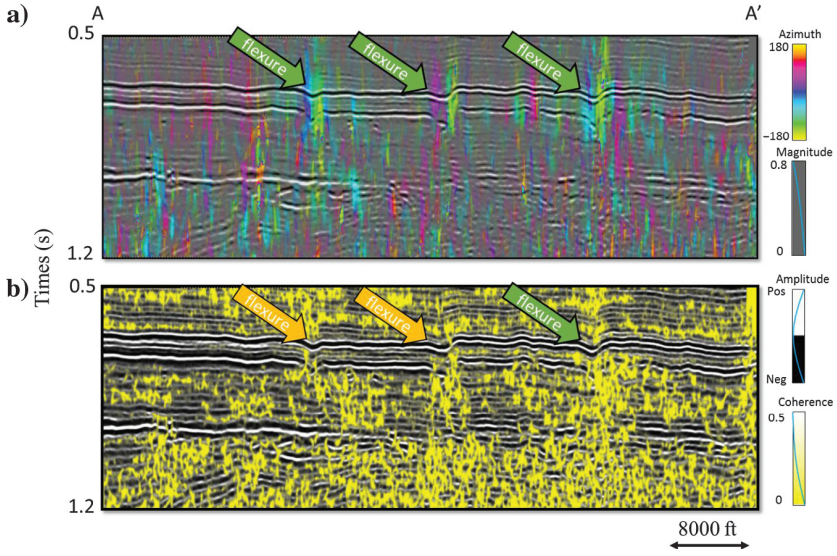

Figure 15. Vertical slices along line AA′ through (a) aberrancy and (b) coherence. Arrows indicate anomalies along the top Marble Falls that are better resolved by aberrancy.

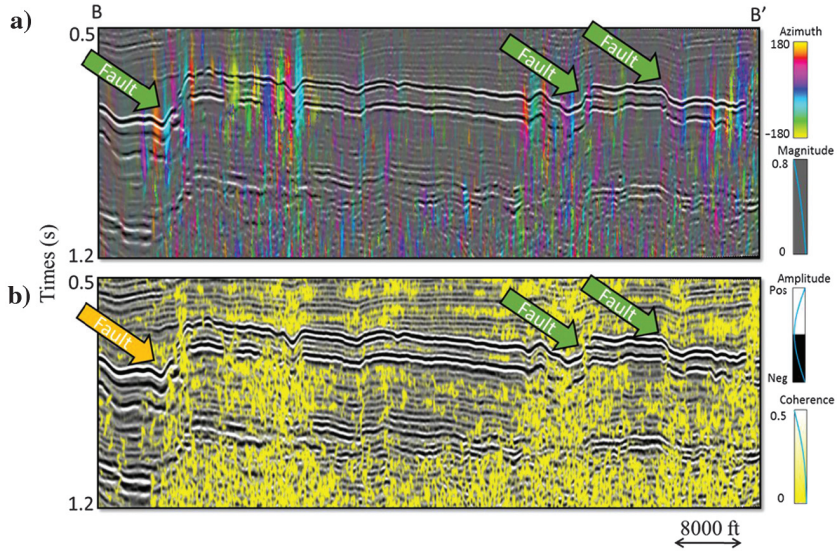

Figure 16. Vertical slices along line BB′ through (a) aberrancy and (b) coherence. Arrows indicate anomalies along the top Marble Falls that are better resolved by aberrancy. The faults in the aberrancy image appear as relatively thin, vertically continuous vertical thin lines, but they appear as less continuous stair-step blotches in coherence.

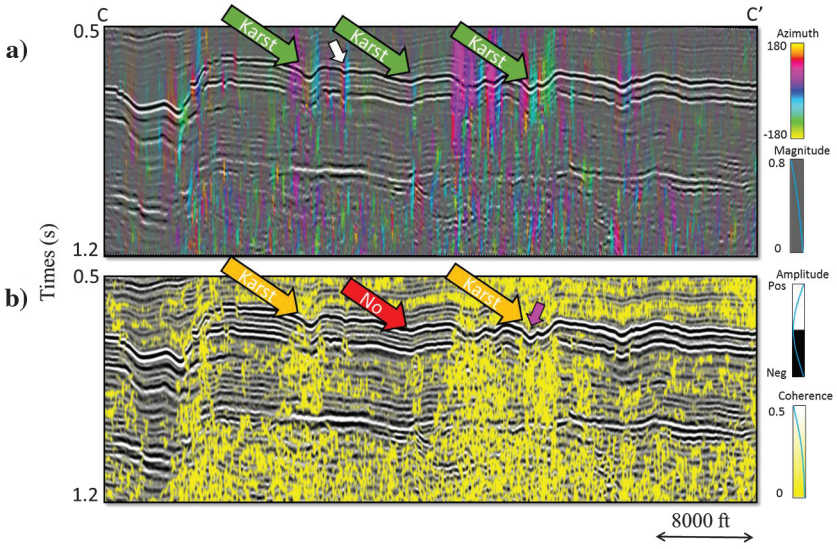

Figure 17. Vertical slices along line CC′ through (a) aberrancy and (b) coherence through several collapse features. Arrows indicate anomalies along the top Marble Falls that are better resolved by aberrancy. The flexure indicated by the magenta arrow in (b) exhibits a 19 ms offset over a distance of 79.2 m (260 ft), whereas the more subtle flexure indicated by the white arrow in (a) exhibits only a 8 ms offset more than 79.2 m (260 ft).

Conclusion

Tectonic forces, diagenetic dissolution, diapirism, and erosion all act to deform stratigraphic layers that originally may have been deposited with relatively featureless surfaces. Although coherence measures disruptions in these surfaces, dip, curvature, and aberrancy measure changes in their orientation and morphology. Lateral changes in dip give use to curvature, whereas lateral changes in curvature give use to aberrancy.

Positive and negative curvature pairs are commonly used to map the footwall and hanging wall of normal faults, bracketing a coherence anomaly. When the fault offset falls below seismic resolution, and the coherence anomaly disappears, the curvature pattern can be used to map the fault further. In general, curvature anomalies are typically juxtaposed to rather than aligned with a fault. In contrast, aberrancy anomalies are aligned with the fault, providing a quantitative measure than can not only be mapped, but that also can be correlated with image logs, production logs, chemical trace data, and other measures of fractures.

Previously limited to computation from picked horizons, we have extended aberrancy to provide volumetric results of uninterpreted seismic data volumes. By using along-wavelength calculations commonly used in volumetric curvature computations implemented as convolution operators in the original unrotated data volume, we obtain results that are numerically stable, computationally efficient, and geologically meaningful.

Although we compute the three aberrancy roots, their value as independent measures has yet to be determined. In contrast, the vector sum of these three roots is easier to understand and interpret. Because it is a vector, total aberrancy images can be azimuthally limited using to highlight and then numerically correlate hypothesized fracture sets to production data.

Although aberrancy will provide superior images of certain geologic features, it will complement rather than supplant other structural attributes such as coherence, curvature, and diffraction imaging. Indeed, when used together, they provide deeper insight into the seismic data volume.

Acknowledgments

We thank the industrial sponsors of the Attribute Assisted Seismic Processing and Interpretation (AASPI) Consortia at the University of Oklahoma for their technical guidance and financial support of this work. Thanks to Marathon Oil Company for a license to their Fort Worth Basin seismic data volume. D. Dewett of BHPBilliton and J. Rich of Devon Energy provided particular geologic motivation and encouragement. All computations were performed using the AASPI software package. We also thank Schlumberger for licenses for research and education the to Petrel 2016, which we used for visualization.

Appendix A

Computation of derivatives in a rotated coordinate system

Reflector dip and the unit normal

Seismic interpreters commonly define reflector dip vector $\mathbf{u}$ in terms of an inline dip component p_1 and crossline dip component p_2 for time-migrated data in units of s/km or s/kft:

$$\mathbf{u} = \hat{\mathbf{x}}_1 p_1 + \hat{\mathbf{x}}_2 p_2 + 1. \tag{A-1}$$

We will assume the x_1-axis of the survey to be north and the x_2-axis to be east, with all azimuths ϕ measured clockwise from the north. Other survey orientations require additional rotations before any of the rotations described below. Computation of curvature and aberrancy requires the conversion of such dips to the depth domain, either through depth migration, depth conversion of a time-migrated data volume, or more commonly, using a single-conversion velocity, resulting in the units of p_1 and p_2 being dimensionless (or more explicitly, in km/km or kft/kft), much as a roofer measures the pitch when installing a new roof. Thus, p_1 measures how many units down the horizon goes for every unit traversed in the x-direction, and p_2 measures how many units down the horizon goes for every unit traversed in the y-direction. The definition of a vector requires a third component, which is a measure of how

many units down one goes for every unit traversed in the x_3-direction. This last value, which is not always obvious, is identically 1.0 for all dips.

Given these definitions, the unit normal to the reflector surface, $\mathbf{n} = (n_1, n_2, n_3)$, where the axes are chosen, such that $n_3 \geq 0$ (Figure A-1), is then

$$\mathbf{n} = \begin{pmatrix} n_1 \\ n_2 \\ n_3 \end{pmatrix} = \frac{1}{(p_1^2 + p_2^2 + 1^2)^{1/2}} \begin{pmatrix} p_1 \\ p_2 \\ 1 \end{pmatrix}. \quad \text{(A-2)}$$

After depth conversion of the vector $\mathbf{p}$, the reflector dip magnitude θ and dip azimuth ϕ are

$$\theta = \text{ACOS}\left[\frac{1}{(p^2 + q^2 + 1^2)^{1/2}}\right] \quad \text{(A-3a)}$$

and

$$\varphi = \text{ATAN2}(p_2, p_1), \quad \text{(A-3b)}$$

where the result of the function ATAN2 ranges between $\pm 180°$.

Derivatives in the original (unrotated) coordinate system

Using indicial notation, the derivative in the $x_l (l = 1, 2, 3)$ direction of vector dip component p_n $(n = 1, 2)$ in the unrotated coordinate system can be written as

$$p_{n,l} = \partial_l p_n, \quad \text{(A-4a)}$$

whereas the second derivatives in the l and $m (m = 1, 2, 3)$ directions are

$$p_{n,lm} = \partial_m \partial_l p_n. \quad \text{(A-4b)}$$

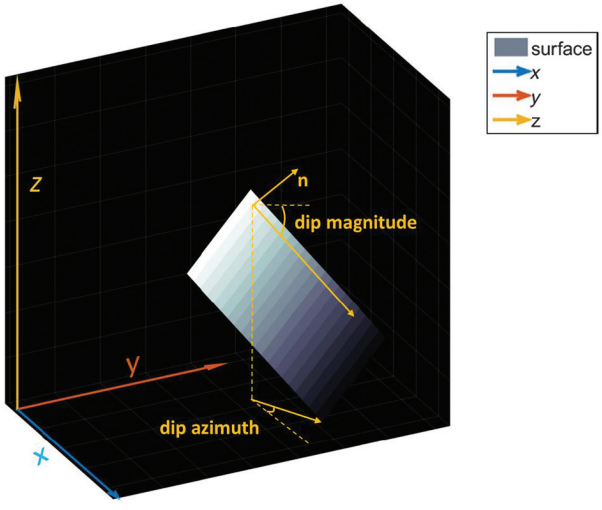

Figure A-1. Schematic diagram showing a reflector surface, $z(x, y)$ (in gray) along with dip magnitude, dip azimuth, and the unit vector $\mathbf{n}$ normal to the reflector surface.

In terms of implementation, we compute the gradient of p_n numerically, using a convolutional operator described by Marfurt (2006). The second derivatives are computed by cascading two first derivative convolution derivative operators. The convolution of the more finally sampled vertical dimension is accelerated by computing the convolution as a multiplication in the vertical wavenumber domain.

The vector dip and its derivatives in the rotated coordinate system

Di and Gao (2016) show that the equations for curvature and aberrancy are much simpler if the data are first flattened about the reflector normal at each voxel. Such flattening requires a rotation $-\varphi$ about the original x_3-axis, followed by a rotation $-\theta$ first about the new x_2' axis. The resulting rotation operator $\mathbf{R}$ is then

$$\begin{bmatrix} p_1' \\ p_2' \\ p_3' \end{bmatrix} = \begin{pmatrix} R_{11} & R_{12} & R_{13} \\ R_{21} & R_{22} & R_{23} \\ R_{31} & R_{32} & R_{33} \end{pmatrix} \begin{pmatrix} p_1 \\ p_2 \\ p_3 \end{pmatrix} = \begin{pmatrix} \cos\theta\cos\varphi & -\cos\theta\sin\varphi & \sin\theta \\ \sin\varphi & \cos\varphi & 0 \\ -\sin\theta\cos\varphi & \sin\theta\sin\varphi & \cos\theta \end{pmatrix} \begin{pmatrix} p_1 \\ p_2 \\ p_3 \end{pmatrix}, \quad \text{(A-5)}$$

where $p_3 = 1$. Writing equation A-5 in indicial notation using the Einstein summation convention (Einstein et al., 1938):

$$p_k' = R_{kn} p_n (k = 1, 2, 3). \quad \text{(A-6)}$$

The gradient ∂_l is a vector operator and can also be rotated:

$$\partial_j' = R_{jl} \partial_l (j = 1, 2, 3), \quad \text{(A-7)}$$

whereas the rotated second derivative operator becomes

$$\partial_i \prime \partial_j \prime = R_{im} \partial_m R_{jl} \partial_l = R_{im} R_{jl} \partial_m \partial_l (i = 1, 2, 3). \quad \text{(A-8)}$$

Applying the operator in equation A-8 to the dip components in equation A-6, the rotated derivatives of p_k' are thus

$$\partial_i' \partial_j' p_k' = R_{im} \partial_m R_{jl} \partial_l R_{kn} p_n = R_{im} R_{jl} R_{kn} (\partial_m \partial_l p_n), \quad \text{(A-9)}$$

where the terms in the parentheses are the previously calculated derivatives in the original, unrotated coordinate system given in equation A-4b. For efficiency, we compute the required derivatives in the unrotated system then using equation A-9.

APPENDIX B

Computing the extrema of apparent aberrancy

Derivation of the roots to the cubic equation

Di and Gao (2014) show that the apparent flexure f_ψ at azimuth ψ in the rotated coordinate system to be

$$f_\psi = \frac{\partial^3 z'}{\partial x_1' \partial x_1' \partial x_1'} \cos^3\psi + 3\frac{\partial^3 z'}{\partial x_1' \partial x_1' \partial x_2'} \cos^2\psi \sin\psi + 3\frac{\partial^3 z'}{\partial x_1' \partial x_2' \partial x_2'} \cos\psi \sin^2\psi + \frac{\partial^3 z\prime}{\partial x_2' \partial x_2' \partial x_2'} \sin^3\psi, \quad \text{(B-1)}$$

where $z'(x_1', x_2')$ is their rotated picked surface. Computing the derivative of f_ψ, with ψ and setting the result to zero results in an equation for three extrema:

$$\frac{df_\psi}{d\psi} = \cos^3\psi \cdot \left[-\frac{\partial^3 z'}{\partial x_1' \partial x_1' \partial x_2'} \tan^3\psi - \left(2\frac{\partial^3 z'}{\partial x_1' \partial x_1' \partial x_2'} - \frac{\partial^3 z'}{\partial x_2' \partial x_2' \partial x_2'} \right) \tan^2\psi + \left(2\frac{\partial^3 z\prime}{\partial x_1' \partial x_2' \partial x_2'} - \frac{\partial^3 z'}{\partial x_1' \partial x_1' \partial x_1'} \right) \tan\psi + \frac{\partial^3 z'}{\partial x_1' \partial x_1' \partial x_2'} \right]. \quad \text{(B-2)}$$

Next, Di and Gao (2014) set $y = \tan\psi$ and define coefficients a, b, c, and d, to obtain a simple cubic equation in s:

$$\frac{df_\psi}{d\psi} = \cos^3\psi (ay^3 + by^2 + cy + d). \quad \text{(B-3)}$$

The coefficients of equation B-3 are third derivatives of the rotated surface z'. In our volumetric implementation, we do not pick any surfaces. The third derivatives of z' in equation B-2 then become the second derivatives of p_1' and p_2', resulting in

$$a = -\frac{1}{2}(\partial_2'\partial_2' p_1' + \partial_1'\partial_2' p_2'), \quad \text{(B-4)}$$

$$b = -(\partial_1'\partial_2' p_1' + \partial_1'\partial_1' p_2' - \partial_2'\partial_2' p_2'), \quad \text{(B-5)}$$

$$c = +(\partial_2'\partial_2' p_1' + \partial_1'\partial_2' p_2' - \partial_1'\partial_1' p_1'), \quad \text{(B-6)}$$

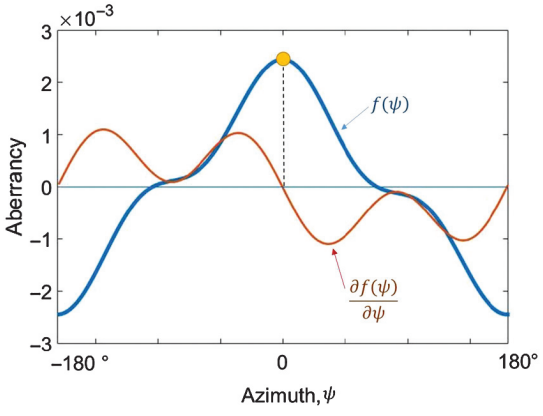

Figure B-1. Flexure $f(\psi)$ showing one independent extremum.

and

$$d = +\frac{1}{2}(\partial_1'\partial_2' p_1' + \partial_1'\partial_1' p_2'). \quad \text{(B-7)}$$

Setting equation B-3 to zero provides the three extrema of the cubic equation. There are multiple special cases that would lead to equation B-3 equals to zeros. The first is the degenerate case, where

$$\cos^3\psi = 0, \quad \text{and} \quad df_\psi/d\psi \equiv 0.$$

In this case, $\psi = 90°$.

For the nondegenerate case, where $\cos^3\psi \neq 0$, one solves the cubic equation

$$ay^3 + by^2 + cy + d = 0. \quad \text{(B-8)}$$

Computation of the roots to the cubic equation

Following Fan (1989), one defines the following variables to facilitate the computation of the roots of equation B-3:

$$A = b^2 - 3ac,$$
$$B = bc - 9ad,$$
$$C = c^2 - 3bd, \quad \text{and}$$
$$\Delta = B^2 - 4AC. \quad \text{(B-9)}$$

There are several cases:

Case 1: $A = B = 0$ (three identical roots):

$$s_1 = s_2 = s_3 = -\frac{b}{3a} \quad \text{(B-10)}$$

Case 2: $A \neq 0, B \neq 0, \Delta > 0$ (only one real root) (Figure B-1):

$$s_1 = \frac{-b - (Y_1)^{1/3} + (Y_2)^{1/3}}{3a}, \quad \text{(B-11)}$$

where

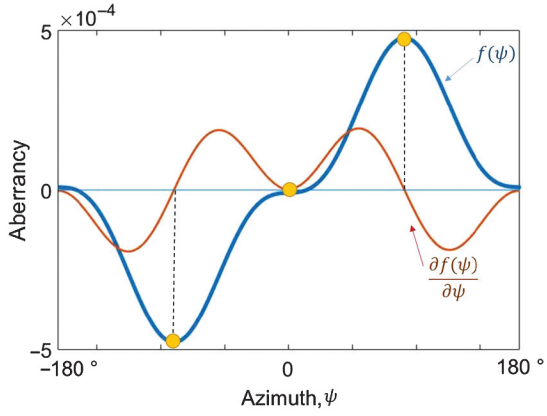

Figure B-2. Flexure $f(\psi)$ showing two independent extrema.

$$Y_1 = Ab + 3a\left(\frac{-B + \sqrt{B^2 - 4AC}}{2}\right) \quad \text{and}$$
$$Y_2 = Ab + 3a\left(\frac{-B - \sqrt{B^2 - 4AC}}{2}\right). \tag{B-12}$$

Case 3: $A \neq 0, B \neq 0, \Delta = 0$ (three real roots, two of which are identical):

$$s_1 = -\frac{b}{a} + \frac{B}{A}$$
$$\text{and} \quad s_2 = s_3 = -\frac{B}{2A}. \tag{B-13}$$

Case 4: $A \neq 0, B \neq 0, \Delta < 0$ (three independent real roots) (Figure B-2):

$$s_1 = \frac{-b - 2A^{1/2}\cos\Lambda}{3a},$$
$$s_2 = \frac{-b + A^{1/2}(\cos\Lambda + \sqrt{3}\sin\Lambda)}{3a}, \quad \text{and}$$
$$s_3 = \frac{-b + A^{1/2}(\cos\Lambda - \sqrt{3}\sin\Lambda)}{3a}, \tag{B-14}$$

where

$$\Lambda = \frac{1}{3}\arccos T \quad \text{and}$$
$$T = \frac{2Ab - 3aB}{2A^{3/2}}. \tag{B-15}$$

The resulting values of ψ represent an azimuth in the rotated plane. To compute ψ projected on the x-y plane of the original unrotated coordinate system, one must first create a vector $\mathbf{q}'$

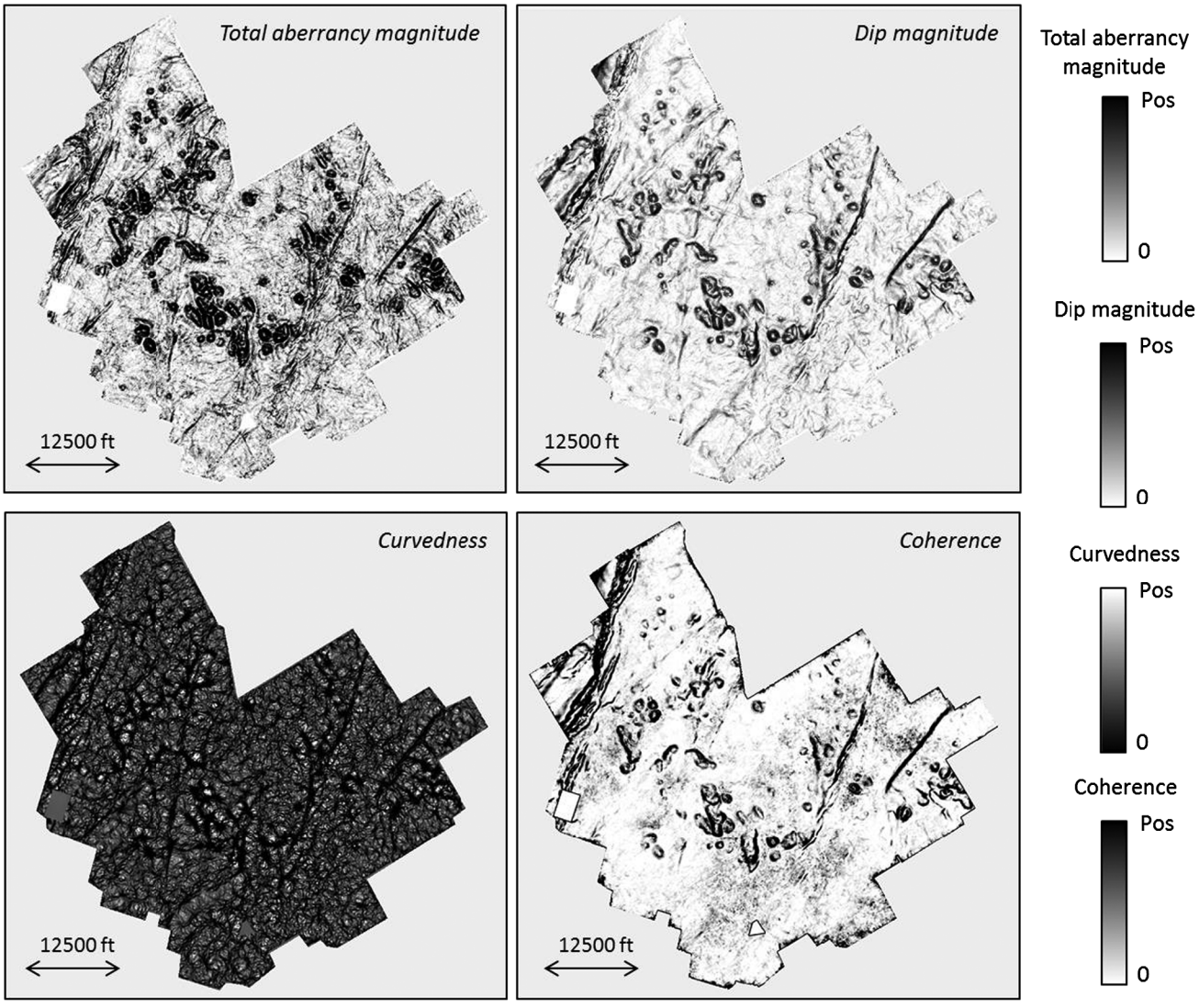

Figure C-1. Horizon slices along the top Marble Falls through the total aberrancy magnitude, dip magnitude, curvedness, and the coherence volume. The total aberrancy is the vector sum of the maximum, intermediate, and minimum aberrancy vectors.

$$\begin{pmatrix} q_1' \\ q_2' \\ q_3' \end{pmatrix} = \begin{pmatrix} \cos\psi \\ \sin\psi \\ 0 \end{pmatrix}, \tag{B-16}$$

and rotate it back using the transpose of **R**

$$q = R^T q'. \tag{B-17}$$

The desired aberrancy azimuth measured from north is then ATAN2(q_2, q_1).

Appendix C

Magnitude of aberrancy

The use of color by interpreters is subjective. Many interpreters prefer to display just the magnitude of aberrancy. We have emphasized the point that aberrancy is a vector, whereby the azimuth shows the orientation of the flexure. However, there are applications (e.g., cor-endering an edge attribute-like aberrancy with impedance inversion or peak frequency), where one would rather use a gray scale. We have included an additional figure that shows coherence, dip magnitude, curvedness, and the magnitude of aberrancy, all plotted against a gray-scale color bar in Figure C-1.

Appendix D

Apparent aberrancy

The maximum aberrancy is larger in magnitude than the intermediate and minimum aberrancy. The problem that we have with aberrancy is that the roots (at least at present) cannot be organized in a manner that separates geologic features, such as k_1 and k_2 do for curvature. As the crossing flexures become larger and smaller, we will encounter situations in which the maximum aberrancy will follow two separate flexures rather than a single flexure that is losing strength when it crosses a second one gaining strength. Our current fix for this issue is to provide a suite of apparent aberrancy images, sorted by azimuthal windows (Figure D-1).

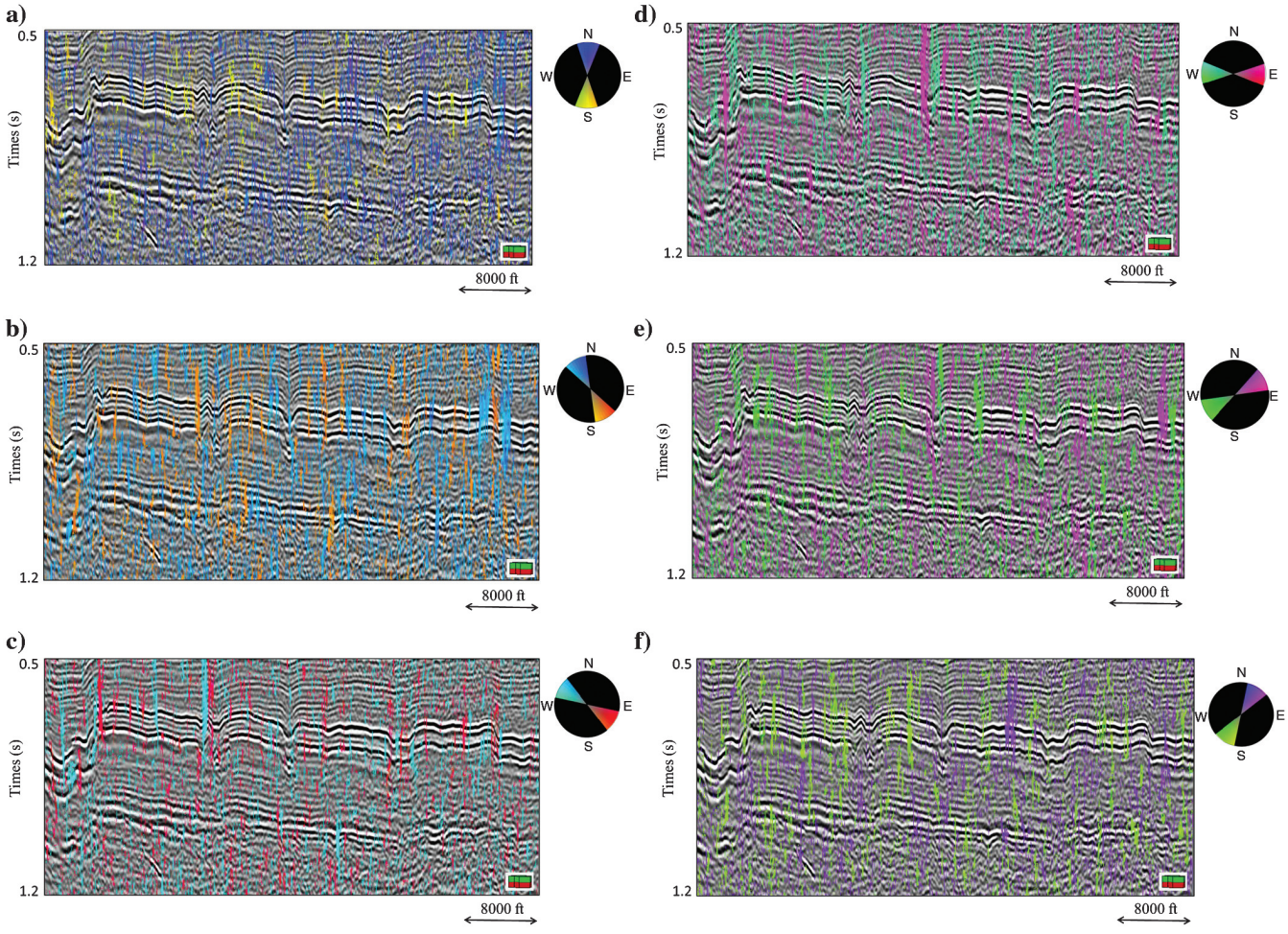

Figure D-1. Because each aberrancy anomaly is described by a magnitude and an azimuth, one can generate a suite of apparent aberrancy by either explicitly filtering the attribute volumes, or as shown in this suite of six images at 30° increments, using opacity resulting in image that show flexure trending at (a) 0° and −180°, (b) 30° and −150°, (c) 60° and −120°, (d) 90° and −90°, (e) 120° and −60°, and (f) 150° and −30°.

References

Borwein, P., and T. Erdélyi, 2012, Polynomials and polynomial inequalities: Springer.

Bruner, K. R., and R. Smosna, 2011, A comparative study of the Mississippian Barnett Shale, Fort Worth Basin, and Devonian Marcellus Shale, Appalachian Basin: Technical Report DOE/NETL/2011/1478, National Energy Technology Laboratory for the United States Department of Energy.

Chopra, S., and K. Marfurt, 2007a, Seismic attributes for prospect identification and reservoir characterization: SEG and EAGE.

Chopra, S., and K. J. Marfurt, 2007b, Volumetric curvature attributes add value to 3D seismic data interpretation: The Leading Edge, **26**, 856–867, doi: 10.1190/1.2756864.

Di, H., and D. Gao, 2014, A new algorithm for evaluating 3D curvature and curvature gradient for improved fracture detection: Computers & Geosciences, **70**, 15–25, doi: 10.1016/j.cageo.2014.05.003.

Di, H., and D. Gao, 2016, Improved estimates of seismic curvature and flexure based on 3D surface rotation in the presence of structure dip: Geophysics, **81**, no. 2, IM13–IM23, doi: 10.1190/geo2015-0258.1.

Einstein, A., L. Infeld, and B. Hoffmann, 1938, The gravitational equations and the problem of motion: Annals of Mathematics, **39**, 65–100, doi: 10.2307/1968714.

Fan, S., 1989, A new extracting formula and a new distinguishing means on the one variable cubic equation: Journal of Hainan Teachers College, **2**, 91–98.

Gao, D., 2013,Integrating 3D seismic curvature and curvature gradient attributes for fracture characterization: Methodologies and interpretational implications: Geophysics, **78**, no. 2, O21–O31, doi: 10.1190/geo2012-0190.1.

Gao, D., and H. Di, 2015, Extreme curvature and extreme flexure analysis for fracture characterization from 3D seismic data: New analytical algorithms and geologic implications: Geophysics, **80**, no. 2, IM11–IM20, doi: 10.1190/geo2014-0185.1.

Joshi, P., and C. Séquin, 2010, An intuitive explanation of third-order surface behavior: Computer Aided Geometric Design, **27**, 150–161, doi: 10.1016/j.cagd.2009.11.003.

Khatiwada, M., G. R. Keller, and K. J. Marfurt, 2013, A window into the Proterozoic: Integrating 3D seismic, gravity, and magnetic data to image subbasement structures in the southeast Fort Worth Basin: Interpretation, **1**, no. 2, T125–T141, doi: 10.1190/INT-2013-0041.1.

Marfurt, K. J., 2006, Robust estimates of 3D reflector dip and azimuth: Geophysics, **71**, no. 4, P29–P40, doi: 10.1190/1.2213049.

Montgomery, S. L., D. M. Jarvie, K. A. Bowker, and R. M. Pollastro, 2005, Mississippian Barnett Shale, Fort Worth basin, north-central Texas: Gas-shale play with multi-trillion cubic foot potential: AAPG Bulletin, **89**, 155–175, doi: 10.1306/09170404042.

Qi, J., B. Zhang, H. Zhou, and K. Marfurt, 2014, Attribute expression of fault-controlled karst — Fort Worth Basin, Texas: A tutorial: Interpretation, **2**, no. 3, SF91–SF110, doi: 10.1190/INT-2013-0188.1.

Rich, J., and K. Marfurt, 2013, Curvature gradient attributes for improved fault characterization: 83rd Annual International Meeting, SEG, Expanded Abstracts, 1319–1323, doi: 10.1190/segam2013-1290.1.

Schot, S. H., 1978, Aberrancy: Geometry of the third derivative: Mathematics Magazine, **51**, 259–275, doi: 10.2307/2690245.

Schuelke, J. S., 2011, Overview of seismic attribute analysis in shale plays: GCSSEPM 31st Annual Bob. F. Perkins Research Conference on Seismic attributes — New views on seismic imaging: Their use in exploration and production, 806–827.

Xuan Qi received an M.S. (2013) in ecology from University of Oklahoma, where she is currently pursuing a Ph.D. as a member of the attribute AASPI consortium. Her current research interests include seismic attributes development, quantitative seismic interpretation, and applying machine learning techniques in the rate of penetration and production prediction analysis.

Kurt J. Marfurt received a Ph.D. (1978) in applied geophysics from Columbia University's Henry Krumb School of Mines in New York, where he also taught as an assistant professor for four years. He joined the University of Oklahoma (OU) in 2007, where he serves as the Frank and Henrietta Schultz professor of geophysics within the ConocoPhillips School of Geology and Geophysics. He worked for 18 years in a wide range of research projects at Amoco's Tulsa Research Center, after which he joined the University of Houston for eight years as a professor of geophysics and the director of the Allied Geophysics Lab. He has received the following recognitions: SEG best paper (for coherence), SEG best presentation (for seismic modeling), as a coauthor with S. Chopra best SEG poster (for curvature) and best AAPG technical presentation, and as a coauthor with R. Perez-Altamar for best paper in *Interpretation* (on a resource play case study). He also served as the SEG/EAGE Distinguished Short Course Instructor for 2006 (on seismic attributes). In addition to teaching and research duties at OU, he leads short courses on attributes for SEG and AAPG. He currently serves as editor-in-chief of the SEG/AAPG publication *Interpretation*. His primary research interest is in the development and calibration of new seismic attributes to aid in seismic processing, seismic interpretation, and reservoir characterization. Recent work has focused on applying coherence, spectral decomposition, structure-oriented filtering, and volumetric curvature to mapping fractures and karst with a particular focus on resource plays.